CSCanada
Advances in Petroleum Exploration and Development
Vol. 14, No. 1, 2017, pp. 18-32
DOI:10.3968/9683

ISSN 1925-542X [Print]
ISSN 1925-5438 [Online]
www.cscanada.net
www.cscanada.org

Uncertainty Analysis of Smart Waterflood Recovery Performance in Clastic Reservoirs

Teeratorn Kadeethum[a],*; Adedapo Noah Awolayo[a]; Hemanta Sarma[a]; Brij Maini[a]; Chalong Jaruwattanasakul[b]

[a]University of Calgary, 2500 University Drive NW, Calgary, AB T2N 1N4, Canada.
[b]Professor, Department of Petroleum Geosciences Engineering, University of Stavanger, Stavanger, Norway.
*Corresponding author.

Supported by the Schulich School of Engineering, University of Calgary Startup Funding.

Received 12 June 2017; accepted 8 August 2017
Published online 26 September 2017

Abstract

In recent years, numerous laboratory studies have documented the benefits of smart waterflooding as an emerging enhanced oil recovery (EOR) process, along with a few successful field applications, notably clastic reservoirs. In most cases, there are undeniable inconsistencies between lab and field results. This process has led to unpredictable outcomes and misleading prediction of smart waterflooding projects. Hence, this work is conducted to evaluate uncertainties in smart waterflooding from laboratory to field-scale. An one-dimensional (1-D) reactive transport model was developed and validated with flooding experiments. Validation shows that combinations of various matching parameters can be used to interpret the experiment. Different realizations lead to different results when extended to 3-D heterogeneous model. The sensitivity of parameters like grid size and heterogeneity in full-field model majorly influences smart waterflooding performance, which is responsible for the inconsistencies. Therefore, these parameters should be considered in field-scale simulation to fully demonstrate the potential of smart waterflooding.

Key words: Enhanced oil recovery; Smart waterflooding; Low salinity waterflooding; Reservoir simulation; Statistical analysis; 3-D heterogeneous model

Kadeethum, T., Awolayo, A. N., Sarma, H., Maini, B., & Jaruwattanasakul, C. (2017). Uncertainty Analysis of Smart Waterflood Recovery Performance in Clastic Reservoirs. *Advances in Petroleum Exploration and Development*, *14*(1), 18-32. Available from: http://www.cscanada.net/index.php/aped/article/view/9683
DOI: http://dx.doi.org/10.3968/9683

INTRODUCTION

For years, waterflooding has been used in oil exploration. However, the role of water chemistry on oil recovery was mainly identified about 60 years ago. It was detected that injection of fresh water into clastic core lead to higher recovery compared to conventional water injection[1-2]. In a 1996 study conducted by Morrow and co-workers, the work was revisited and there, the concept of smart water emanated. Ever since then, a great chunk of experimental studies have been carried out to assess the effects of water composition and salinity on oil recovery[1-13]. Diverse opinions exist among researchers on the mechanism responsible for the smart waterflood recovery process, though wettability alteration has been proposed to be the fundamental mechanism.[14] Though more than 500 experiments have been conducted, the main factors that influence smart waterflooding behaviour are still unclear[15].

Even though the positive response has been reported for smart waterflooding in core-scale experiments, when these results are applied to the field-scale, the outcomes range from neutral to negative. Thus, only a few successful field trials have been reported[16-18]. While developing tools that can efficiently screen, design and optimize smart waterflood in field-scale, unfavorable situations can arise because of assumptions applied when extending core-scale model to 3-D model. Moreover, there is always more than one realization that can describe and interpret coreflooding results. Each realization may lead to different results when extended

to 3-D. Therefore, these issues should be addressed and discussed to evaluate the potential of smart waterflooding in full-field.

Waterflooding performance in the field-scale is often a function of parameters like mobility ratio, dip angle, formation connectivity, fractures, areal and vertical permeability distribution, flood pattern, injection/ production rate, barriers, and capillary pressure[19]. Moreover, grid size can significantly influence EOR performance[20-22]. The main focus of this study is the effect of heterogeneity and grid size on recovery performance. Therefore, we tuned this paper to assess uncertainties from the core- to field-scale that can alter smart waterflooding performance by numerical simulation and statistical analysis.

1. METHODOLOGY

There are two parts in this section. The first part describes general methods for associated equations that are used throughout this study while in the second part, the experiment data utilized for model validation and 3-D extended model are discussed.

1.1 Statistical Analysis

We used one-way analysis of variance (ANOVA) to determine whether the means of each level of variables differs with 95% confidence interval. Subsequently, we utilized Tukey comparison to identify the difference between each pair of variable levels.

The ANOVA examines the effects of these variables on the process performance. Sums of squares are often used in ANOVA tests to summarize the partitioning of the variation in the process performance between changes in the independent variables and random error (sum of squares of errors). The various components of the sum of squares can be split as highlighted below, with their associated formulas employed in ANOVA calculation:

○ Degrees of freedom for the variables or factors

$$v_F = r\text{-}1. \tag{1}$$

○ Sum of squares for the factors

$$SSF = \sum n_i(\bar{y}_i - \bar{y}_{..})^2. \tag{2}$$

○ Mean squares for the factors

$$MSF = \frac{SSF}{v_F}. \tag{3}$$

○ Degrees of freedom for the errors

$$v_E = n_T - r\ . \tag{4}$$

○ Sum of squares for the errors

$$SSE = \sum_i \sum_j \left(y_{ij} - \bar{y}_i\right)^2\ . \tag{5}$$

○ Mean squares for the errors

$$MSE = \frac{SSE}{v_E}\ . \tag{6}$$

○ Degrees of freedom for the total data

$$v_T = n_T - 1\,. \tag{7}$$

○ Sum of squares for the total data

$$SST = \sum_i \sum_j \left(y_{ij} - \bar{y}_{..}\right)^2\ . \tag{8}$$

○ Mean squares for the total data

$$MST = \frac{SST}{v_T}. \tag{9}$$

Where,

MSE, MSF, MST = mean of square of errors, factors and total respectively

SSE, SSF, SST = sum of square of errors, factors and total respectively

v_E, v_F, v_T = degree of freedom of errors, factors and total respectively

n_i= number of data in i^{th} level

n_T = number of data

$\bar{y}_i$ = mean of the i^{th} level

y_{ij} = value of the j^{th} observation at the i^{th} level

$\bar{y}_{..}$ = mean of all observations

r = number of levels of factors

Here, the following null and alternative hypothesizes were tested for the ANOVA:

H_0*: Each level of factor has the same mean*

H_1: *At least one mean is not equal to other means*

The validity of the null hypothesis was verified by considering *F*-test statistic, which is calculated using Equation 10. The null hypothesis can be rejected if the obtained result does not follow an *F*-distribution with and degrees of freedom

$$F = \frac{MSF}{MSE}\ . \tag{10}$$

When the *F*-test statistic is larger than the critical value obtained from *F*-distribution, the null hypothesis is rejected, which implies that at least one of the means differs from others. Then, we proceeded to perform Tukey multiple comparisons to estimate the difference between means of each level of factors using Equation (11).

$$\bar{y}_i - \bar{y}_j \pm t\left(1 - \frac{\alpha}{2};\ n_T - r\right) s\sqrt{\frac{1}{n_i} - \frac{1}{n_j}}\ . \tag{11}$$

Where,

$\bar{y}_j$ = mean of the j^{th} level

t = from the *t*-distribution with degrees of freedom

α = significant level

n_j = number of data in j^{th} level

s = standard deviation

1.2 Numerical Simulation

Generalized Equation of State Model (GEM) is used to simulate multicomponent multiphase flow occurring in combination with geochemical reactions. This simulator

is selected because of its flexibility and accuracy to model reactive transport systems. Moreover, this coupled module was validated by Dang[14] and Kadeethum[23]. Three types of chemical reactions are considered in this study: (i) intra-aqueous reactions (Equations (12)-(16)), (ii) mineral dissolution/precipitation reactions (Equations 17 and 18), and (iii) ion exchange reactions (Equations (19) and (20)) representing smart waterflood behavior, as described in works of various authors[14, 23-26]. The reaction sets are:

$$NaCl \leftrightarrow Na^+ + Cl^- , \quad (12)$$

$$CaCl_2 \leftrightarrow Ca^{2+} + 2Cl^- , \quad (13)$$

$$MgCl_2 \leftrightarrow Mg^{2+} + 2Cl^- , \quad (14)$$

$$OH^- + H^+ \leftrightarrow H_2O , \quad (15)$$

$$CO_2 + H_2O \leftrightarrow H^+ + HCO_3^- , \quad (16)$$

$$Dolomite + 2H^+ \leftrightarrow Ca^{2+} + 2HCO_3^- + Mg^{2+}, \quad (17)$$

$$Calcite + H^+ \leftrightarrow Ca^{2+} + HCO_3^- , \quad (18)$$

$$Na^+ + 0.5(Ca - X_2) \leftrightarrow (Na - X) + 0.5Ca^{2+} , \quad (19)$$

$$Na^+ + 0.5(Mg - X_2) \leftrightarrow (Na - X) + 0.5Mg^{2+} . \quad (20)$$

For the intra-aqueous reactions, the chemical reaction is in thermodynamic equilibrium when the forward reaction rate is equal to the backward reaction rate. This implies that the equality condition in Equation (21) must be satisfied:

$$Q_\alpha = K_{eq} = \prod_{i=1}^{n} (a_i)^{\upsilon_{i\alpha}} \qquad for\ \alpha = 1, \ldots\ldots, R_{ia} . \quad (21)$$

Where

Q_α = the activity productof the aqueous reaction,

K_{eq} = the equilibrium constant values mostly tabulated as a function of temperature

R_{ia} = the number of intra-aqueous reactions

a_i = activity of the ith component

n = total number of components in aqueous phase

$\upsilon_{i\alpha}$ = valence of the i^{th} component in the aqueous reaction

In this study, aqueous components are considered to deviate from ideal mixing, such that activity coefficients used in obtaining the activity of each component in Equation (22) are calculated using B-dot activity model[27], as shown in Equation (23).

$$a_i = \gamma_i m_i \qquad for\ i = 1, \ldots\ldots, n , \quad (22)$$

$$log\ \gamma_i = -\frac{A_\gamma z_i^2 \sqrt{I}}{1 + \dot{a}_\iota B_\gamma \sqrt{I}} + \dot{B} I , \quad (23)$$

with

$$I = \frac{1}{2} \sum_{i=1}^{n} m_i\, z_i^2 . \quad (24)$$

Where,

$\dot{a}_i$ = ion size of i^{th} component

I = total charge

m_i = molality of the i^{th} component

z_i = charge of the i^{th} component

A, B, and $\dot{B}$ = temperature dependent parameters in the B-dot model

γ_i = activity coefficient the i^{th} component

However, rate-dependent reactions were considered for the mineral reactions and their law of mass action written based on transition state theory is as follows:

$$r_\beta = k_\beta \dot{A}_\beta \left(1 - \frac{Q_\beta}{K_{eq}}\right) \quad for\ \beta = 1, \ldots\ldots, R_m . \quad (25)$$

Where, r_β is the rate of reaction, k_β is the rate constants, $\dot{A}_\beta$ is the mineral reactive surface area, Q_β is the activity product, R_m is the number of mineral surface reactions and K_{eq} is the equlibrum constants; all for mineral surface reaction β.

Like the intra-aqueous reactions, the ion exchange reactions were assumed to be in equilibrium satisfying the condition of Equation (21). However, instead of activity, equivalent fractions of exchangeable species (Equation (26)) were used to define the equilibrium relationships (Equation (27)) with selectivity factor. An example of ion exchange reaction in Equation (19) is as follows:

$$\psi_{(Na-X)} = \frac{N_{(Na-X)}}{\phi CEC} \quad ; \quad \psi_{(Ca-X_2)} = \frac{2N_{(Ca-X_2)}}{\phi CEC} \quad ; \quad CEC = \frac{1}{\phi} \sum_{i=1}^{n_{ex}} N_{(i-X)} z_i , \quad (26)$$

$$Q_{ex} = K_{Na|Ca} = \frac{\psi_{(Na-X)} [a_{Ca^{2+}}]^{0.5}}{\left[\psi_{(Ca-X_2)}\right]^{0.5} a_{Na^+}} . \quad (27)$$

where ψ_i is the equivalent fraction of i^{th} exchangeable species, ϕ is the porosity, $N_{(i\text{-}X)}$ is the moles of i^{th} exchangeable species, is the cation exchange capacity, is the selectivity factor for the reaction in Equation (19), Q_{ex} is the ion-exchanged activity product and n_{ex} is the total number of exchangeable components.

All these equations were coupled with the transport equation and solved numerically as described by Nghiem et al.[28] and Awolayo et al.[26]. The governing equation for the transport of i^{th} component through the porous rock is shown in Equation 28. The first term of the governing equation denotes the components' mass accumulation, while the second term denotes components' convective and dispersive transport. The third and fourth term denotes the components' equilibrium and rate dependent reaction respectively, and the last term denotes source/sink.

$$V_b \frac{\partial N_i}{\partial t} + V_b \sum_{j=o,g,a} \vec{\nabla} \cdot \left(\xi_j y_{ij} u_j - \phi s_j \xi_j D_{ij} \nabla y_{ij} \right) - V_b \sigma_{i,a} - V_b \sigma_{i,m} - q_i = 0 \,, \tag{28}$$

where is the moles per unit bulk volume of the i^{th} component; V_b is the bulk volume; q_i is the molar rate of source/sink term for the i^{th} component;t is the time; y_{ij} and D_{ij} are the molar fractions and diffusion/dispersion coefficients of the i^{th} component in j^{th} phase; ξ_j, s_j and u_j are the molar densities, saturation and velocity of the j^{th} phase; $\sigma_{i,a}$ and $\sigma_{i,m}$ are net moles per unit bulk volume per unit time due to equilibrium-controlled and rate-controlled reactions respectively.

For this study, aqueous phase Ca^{2+} concentration is selected as the interpolant. Equation (29) present the interpolating equation used in this simulation. This interpolation process mimics the wettability alteration behaviour as described by various authors[29,14, 26]. In this study, we used two sets of relative permeability to mimic wettability alteration.

$$k_{r\,\mathrm{int}} = \omega\, k_{r\,\mathrm{set\,1}} + (1-\omega) k_{r\,\mathrm{set\,2}} \,, \tag{29}$$

with

$$\omega = \frac{m_{\mathrm{final}} - m_{(x,t)}}{m_{\mathrm{final}} - m_{\mathrm{initial}}} \,. \tag{30}$$

Where,

ω = interpolant

m_{final}= arbitrarily selected final Ca^{2+} concentration

m_{initial}= arbitrarily selected initial Ca^{2+} concentration

$m_{(x,t)}$= current value of Ca^{2+} concentration calculated at the corresponding time-step

1.3 Field-Scale Modeling

Heterogeneity in the 3-D model is generated by the Simulation Gaussian Simulation (SGS). SGS is a well-accepted method as it better represents geological setting than simple interpolation. In simple interpolation, only the mean of uncertainties is considered, while in SGS, both mean and variance are considered. Key steps of the procedure are in the conceptual flow diagram in Figure 1.

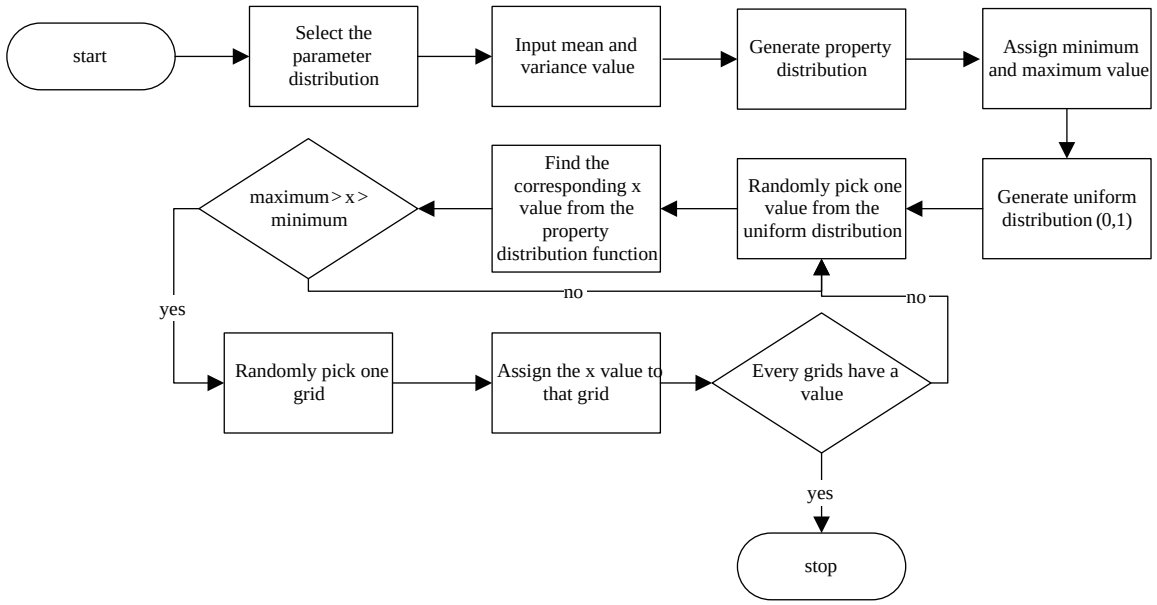

Figure 1
SGS Flow Chart (Adapted From Reference [30])

Line drive pattern with two producers and two injectors was used for the 3-D model, as shown in Figure 2.

CEC is a function of clay content and organic material in the rock as shown in Equation (31)[31]. However, Dang[14] proposed a new regression model based on the experimental data of Seilsepour and Rashidi (2008), as shown in Equation (32). In this study, we utilized Equation (31) to calculate the *CEC* value. Furthermore, clay fraction is assumed to be a function of the maximum porosity and the porosity of each grid block[32] as specified in Equation (33). However, *CEC* used in the simulation model is calculated in eq/m^3 of pore volume (PV) instead of meq/kg (Equation (34)).

CEC=700 × (clay fraction)+3500 × (organic carbon fraction) , (31)

CEC=628.58 × (clay fraction)+48.863 , (32)

$$\text{clay fraction}_{i,j,k} = \phi^1_{\max} - \phi^1_{i,j,k} \,, \tag{33}$$

$$CEC_0 = \frac{10^{-3} \rho_r (1 - \phi^1_{i,j,k})}{\phi^1_{i,j,k}} \times CEC \,. \tag{34}$$

Where,

CEC = cation exchange capacity in meq/kg

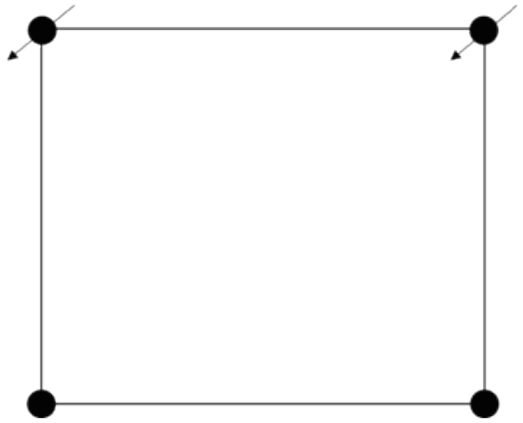

Figure 2
Line Drive Flood Pattern

CEC_0 = cation exchange capacity in eq./m^3 of PV
i,j,k = grid block index
ρ_r = rock density
$(x)^1_{(y)}$ = the first time step

Permeability in the *i*-direction was obtained using Timur[33] correlation for oil-bearing zones (excluding transition zones) as shown in Equation (35). The permeability reported in experimental studies by Kozaki[10] was assumed for the average permeability in the *i*-direction for the 3-D model. While permeability in *j* and *k*-directions was assumed same and ten-times lesser than that in the i-direction, respectively.

$$K = 8581\frac{\phi^{4.4}}{s_{wi}^2}. \quad (35)$$

Where,
K = permeability
s_{wi} = initial water saturation

Relative permeability tables are established by Equations (36) and (37) for water relative permeability and oil relative permeability, respectively. Kozaki[10] only reported the end-point relative permeability; therefore, the curves generated by these equations are used in both coreflooding validation and 3-D model.

$$k_{ro} = k_{ro}^*\left(\frac{s_o - s_{or}}{1 - s_{wi} - s_{or}}\right)^{n_o}, \quad (36)$$

$$k_{rw} = k_{rw}^*\left(\frac{s_w - s_{wi}}{1 - s_{wi} - s_{or}}\right)^{n_w}. \quad (37)$$

Where,
k^*_{rw} = endpoint water relative permeability
k^*_{ro} = endpoint oil-water relative permeability
n_w = Corey exponent of water relative permeability set
n_{ow} = Corey exponent of oil-water relative permeability set
s_w = water saturation
s_o and s_{or} = oil saturation and residual oil saturation, respectively

1.4 Coreflooding Validation

Experimental studies by Kozaki[10] were selected to validate core-scale model, and subsequently extend the result to 3-D model by SGS. Kozaki[10] performed three experiments, (i) low-salinity waterflooding (ii) low-salinity polymer flooding in semi-tertiary mode, and (iii) low-salinity polymer flooding in tertiary mode. In this study, only the first set of experiment is validated and discussed, because incorporating a polymer component in the model is out of the scope of the present study.

The first round of experiment utilized the procedures shown in Figure 3. The difference between two parts of the test is the ageing time. In this validation, only the first section of the experiment was selected. The core that was used in this study is a Berea sandstone core, and the properties are shown in Table 1. The fluid properties are summarized in Table 2 and Table 3. Further details can be found in Kozaki[10]. The flow simulation mimicked the experimental result by simulating low-salinity waterflooding 1, as shown in red in Figure 3.

Table 1
Core Properties for Low-Salinity Waterflooding[10]

Length	11.73	inch
Diameter	1.5	inch
Bulk volume	339.67	mL
Pore volume	61.81	mL
Porosity	18.2	%
Permeability to air	137.52	mD
Permeability to brine	83.03	mD
Clay content	5	% by weight
Flow velocity	0.1	mL/min
Volume	9.4	PV

Table 2
Fluid Properties for the Experiment at 85°C – SFB[10]

Synthetic Formation Brine (SFB)					
Concentration					Viscosity
(ppm)					(cP)
NaCl	KCl	$CaCl_2$	$MgCl_2$-$6H_2O$	TDS	0.47
28,620	650	2,710	3,890	35,870	

Table 3
Fluid Properties for the Experiment at 85 °C – LSB and Crude Oil[10]

Low-Salinity Brine (LSB)			Crude oil (Crude A)
Concentration		Viscosity	Viscosity
(ppm)		(cP)	(cP)
NaCl	TDS	0.47	12
1,000	1,000		

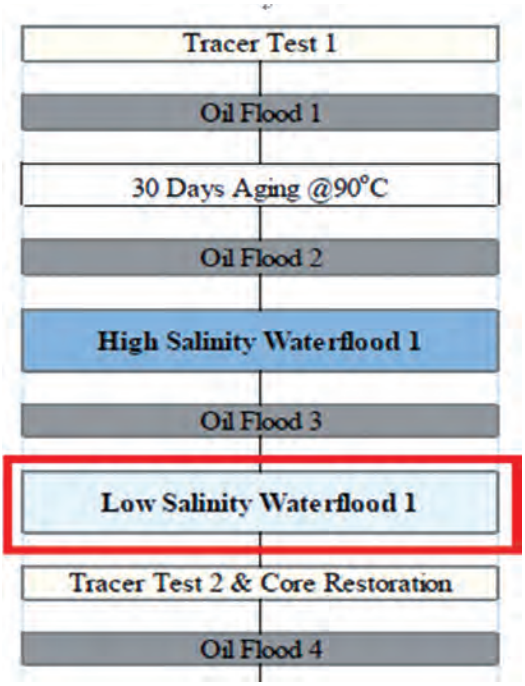

Figure 3
Low-Salinity Waterflooding Procedure[10]

In the experiment, synthetic oil reported has a viscosity of 12 cP at 85℃, which is the only oleic property reported. The relative permeability set used in this simulation is shown in Table 4 for the high-salinity and low-salinity waterflooding set. The matching parameters and their sources of data are shown in Table 5 and Table 6.

Table 4
Relative Permeability Data for High-Salinity Waterflooding and Low-Salinity Waterflooding

Parameter	High-salinity value	Low-salinity value
s_{oi}	0.78	0.74
k_{row} @ s_{oi}	0.45	0.48
s_{or}	0.39	0.35
k_{row} @ s_{or}	0.00	0.00
s_{wi}	0.22	0.26
k_{rw} @ s_{wi}	0.00	0.00
s_{wr}	0.61	0.65
k_{rw} @ s_{wr}	0.03	0.01

Table 5
Matching Parameters for the History-Matching Process

Parameter	
Corey's exponent for oil phase - high salinity	Corey's exponent for oil phase - low salinity
Corey's exponent for water phase - high salinity	Corey's exponent for water phase - low salinity
Activation energy - calcite	Activation energy - dolomite
Reaction surface area - calcite	Reaction surface area - dolomite
Selectivity coefficient - Na & Ca	Selectivity coefficient - Na & Mg

Table 6
Matching Parameters and Their References

Parameter	Reference
Corey's exponent	Brooks & Corey (1964)
Activation energy	Schott et al. (1989)
Reaction surface area	Liu & Yang (2015)
Selectivity coefficient	Appelo & Postma (2005)

2. RESULTS AND DISCUSSIONS

This section covers two parts. The first part describes coreflooding validation results and mart waterflooding uncertainties in the core-scale. The second part shows smart waterflooding uncertainties in the field-scale (grid size and heterogeneity effects).

2.1 Coreflooding Validation and Uncertainties

The experimental results—namely oil recovery, oil cut, injection pressure, and effluents' concentration (Na^+ Ca^{2+} Mg^{2+})—are compared against the simulation results. A total of 23,000 cases was simulated, however, only five best cases are presented in this report. Their results are compared with the experimental data in Figure 4 for oil recovery, in Figure 5 for oil cut, in Figure 6 for injection pressure, in Figure 7 for effluent (Ca^{2+}) concentration, in Figure 8 for effluent (Mg^{2+}) concentration, and lastly, in Figure 9 for effluent (Na^+) concentration. The model was set up to mimic experiment conducted by Kozaki[10], as previously discussed.

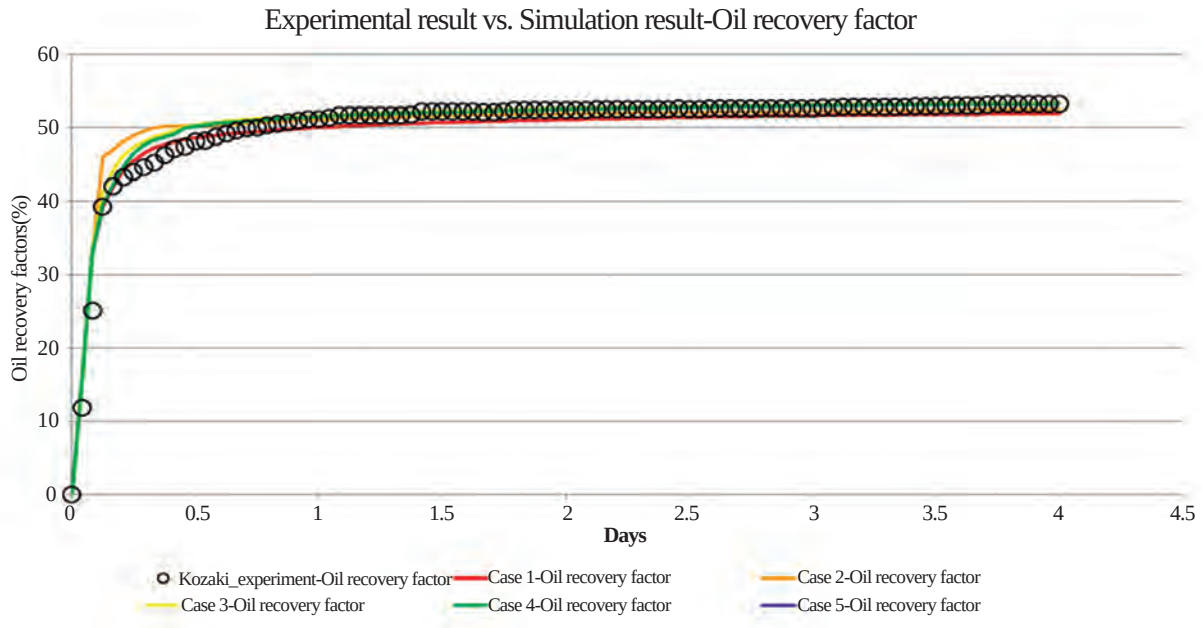

Figure 4
Simulation Results Compare With an Experimental Result: Oil Recovery

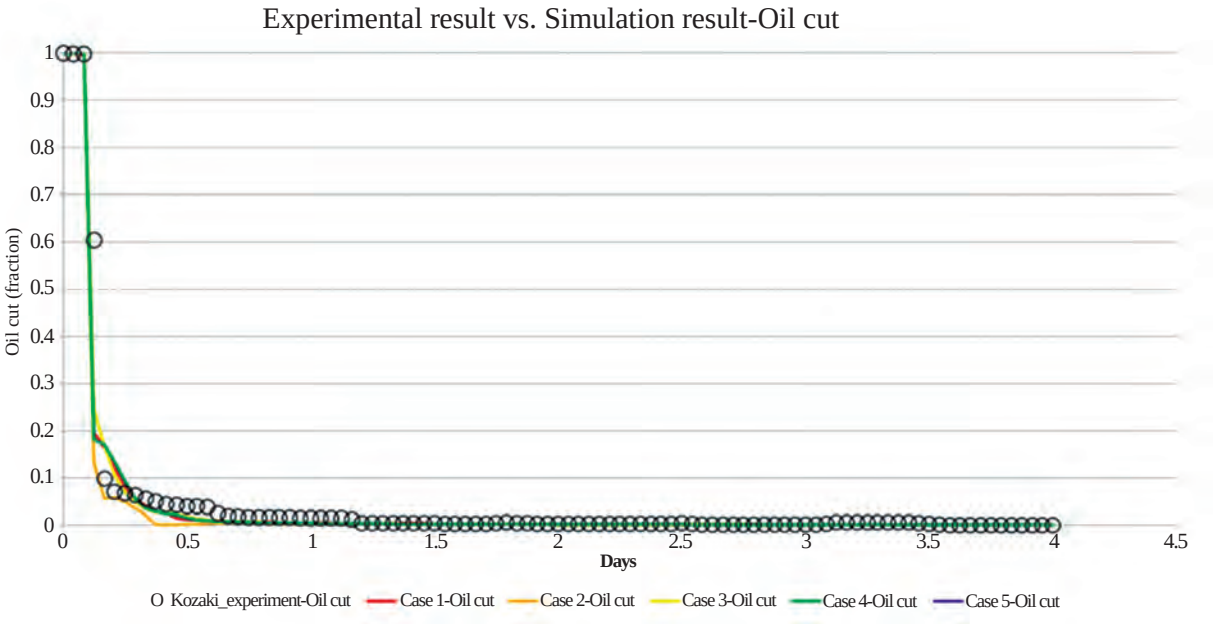

Figure 5
Simulation Results Compare With an Experimental Result: Oil Cut

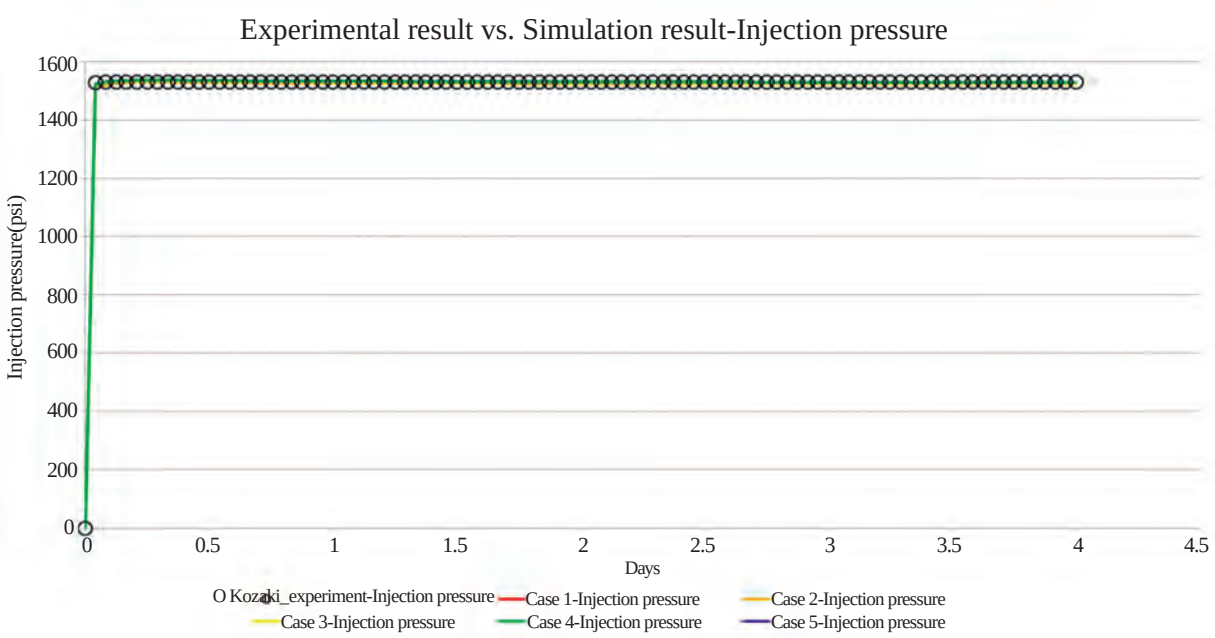

Figure 6
Simulation Results Compare With an Experimental Result: Injection Pressure

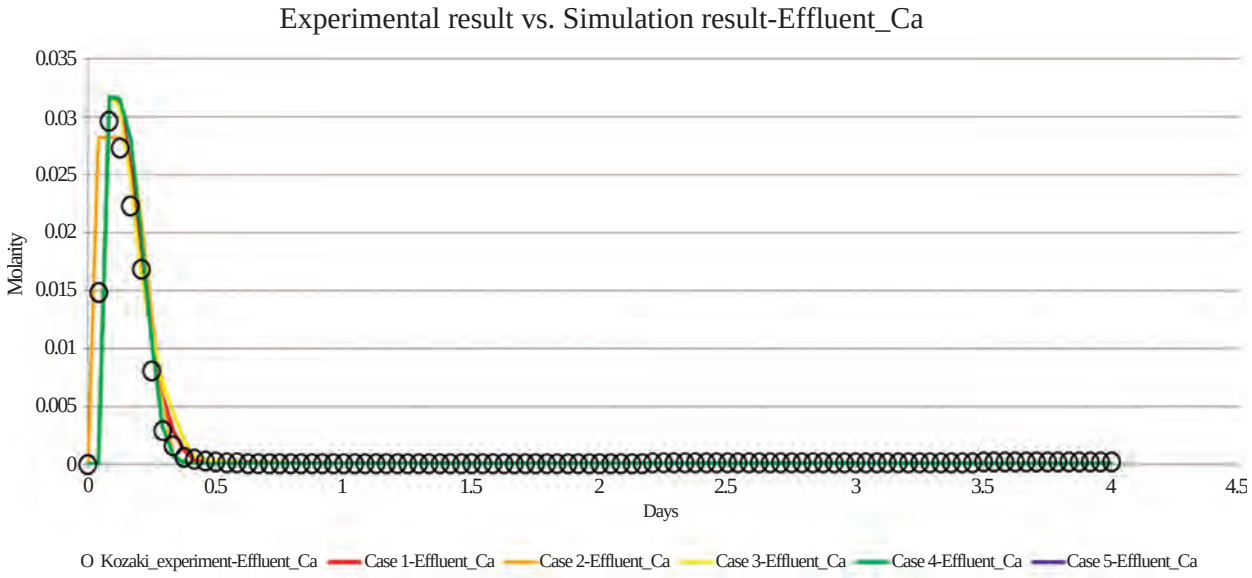

Figure 7
Simulation Results Compare With an Experimental Result: Effluent (Ca^{2+}) Concentration

These simulated results excellently replicated experimental data. However, for Mg^{2+} effluent concentration, four out of five simulated results did not capture the early effluent behaviour. However, one of them excellently replicated the trend. The best case was extended to the 3-D simulation result for further analysis. The result of this extension is shown and discussed in following section.

The matching parameters summary is shown in Table 8. From the figures presented above, all five cases produced reasonable results compared to the experiment. However, their matching parameters highlighted in Table 8 vary significantly. This shows that there is more than one set of solution to capture the smart waterflooding performance. Hence, it is essential to analyze many realizations to cover these range of the uncertainties. This is because all these cases may give different results when extended to 3-D model.

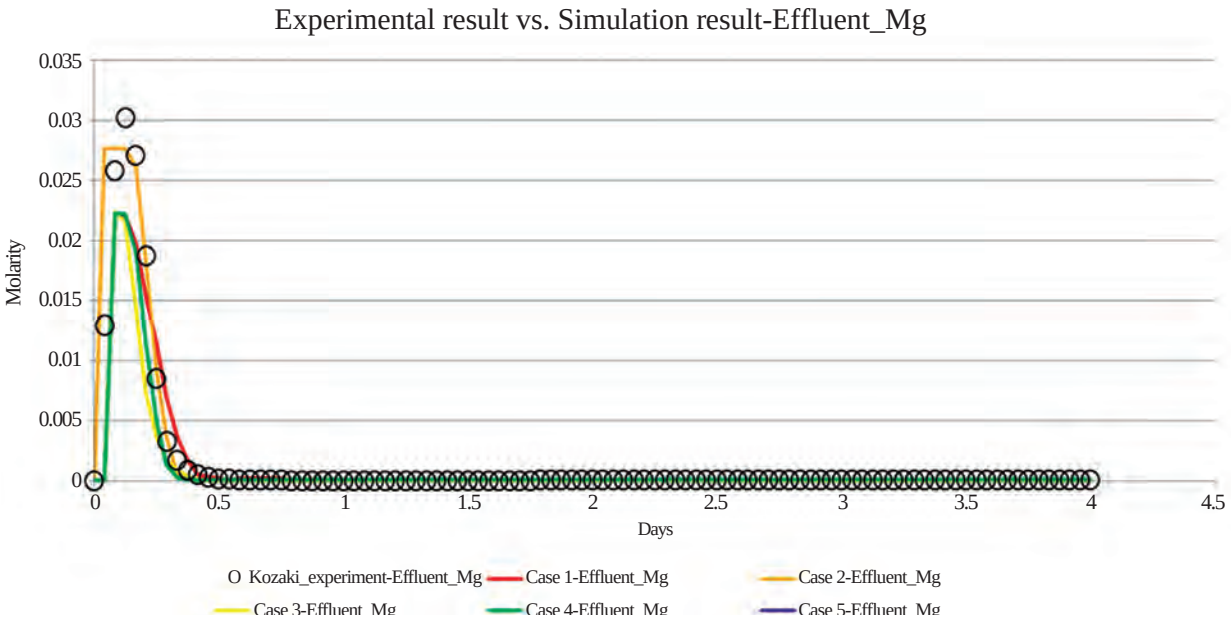

Figure 8
Simulation Results Compare With an Experimental Result: Effluent (Mg^{2+}) Concentration

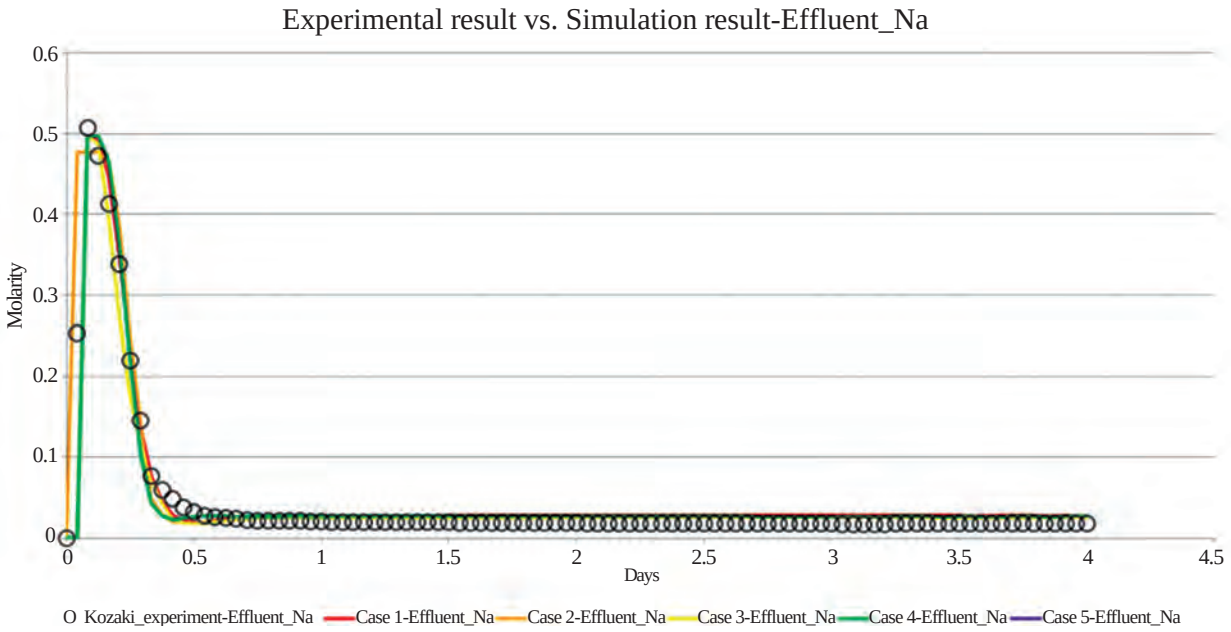

Figure 9
Simulation Results Compare With an Experimental Result: Effluent (Na^{+}) Concentration

Table 7
Matching Parameters Summary

	Case 1	Case 2	Case 3	Case 4	Case 5
Corey's exponent for oil phase - high salinity	3.75	4.00	2.22	3.82	3.69
Corey's exponent for oil phase - low salinity	3.57	3.63	3.02	3.33	3.39
Corey's exponent for water phase - high salinity	1.12	1.30	1.43	1.06	1.25
Corey's exponent for water phase - low salinity	3.32	1.98	3.88	3.27	2.49
Activation energy - calcite	36529	52337	4550	40374	52337
Activation energy - dolomite	41229	31402	45074	48065	39947

To be continued

Continued

	Case 1	Case 2	Case 3	Case 4	Case 5
Reaction surface area - calcite	147.9	141.8	50.0	133.7	115.3
Reaction surface area - dolomite	74.5	86.7	113.3	90.8	90.8
Selectivity coefficient - Na & Ca - lower temp.	0.014	0.009	0.010	0.015	0.013
Selectivity coefficient - Na & Ca - higher temp.	0.455	0.247	0.676	0.700	0.161
Selectivity coefficient - Na & Mg - lower temp.	0.014	0.009	0.005	0.007	0.007
Selectivity coefficient - Na & Mg - higher temp.	0.455	0.418	0.247	0.382	0.541

2.2 Uncertainties in the Field-Scale

In this section, we present two parameters that affect and cause uncertainties in smart waterflooding process. The first one is grid size, and the second one is heterogeneity.

2.2.1 Grid Size Effect on Smart Waterflooding

In this part, grid size effect on smart waterflooding was analyzed, and the optimized grid volume was identified. This sensitivity analysis uses one factor, grid volume; with seven levels: 125, 250, 500, 625,781.25, 1,000, and 1,562.50 m^3. Multiple realizations were generated by SGS, as mentioned in the methodology section. We divided the analysis into three: (i) grid size impact on oil recovery, (ii) grid size impact on material balance error, and (iii) grid size impact on simulation time.

This study utilized a normal distribution with 0.18 mean and 0.03 variance for the porosity distribution. Moreover, permeability and CEC distribution were applied based on previous discussions (Equations (30)-(34)) The distance between producers and injectors was fixed at 200 m., and the flood pattern is a line drive with two injectors and two producers. The simulation time was set to 20 years with injection and production pressures of 1600 psi and 150 psi, respectively. Other variables like (i) relative permeability curves, (ii) geochemical reactions and their constants, (iii) rock properties, and (iv) fluid properties—are obtained based on the history-matched result of experimental data by Kozaki[10].

The result of one-way ANOVA analysis between oil recovery and grid size is shown in Table 8. At a significant level of 0.05, the null hypothesis was rejected because the F-value was greater than critical F-value of 2.122, which means that at least one of the mean differs from others. Consecutively, we performed a Tukey comparison and presented the results in Figure 10. It can be observed that two groups exhibit a statistically significant oil recovery difference: (i) red shade consisted of 125 to 625 m^3 grid volume, and (ii) green shade consisted of 781.25 to 1,562.50 m^3 grid size. Furthermore, when the grid volume increased, the oil recovery also increased, which could lead to a misinterpretation of smart waterflooding performance. The smaller grid size represents better and accurate geological properties distribution. However, it also requires more computational time. Therefore, to optimize simulation time without sacrificing accuracy, we selected the largest grid size with the same oil recovery as the smallest grid size (i.e. the largest grid size in the red shade in Figure 10).

Table 8
Grid Size Influence: Oil Recovery – ANOVA Result

Source	Degree of freedom	Sum of squares	Means squares	*F* value	*P* value
Volume	6	2,219	369.76	33.30	<<0.001
Error	662	7,350	11.10		
Total	668	9,568			

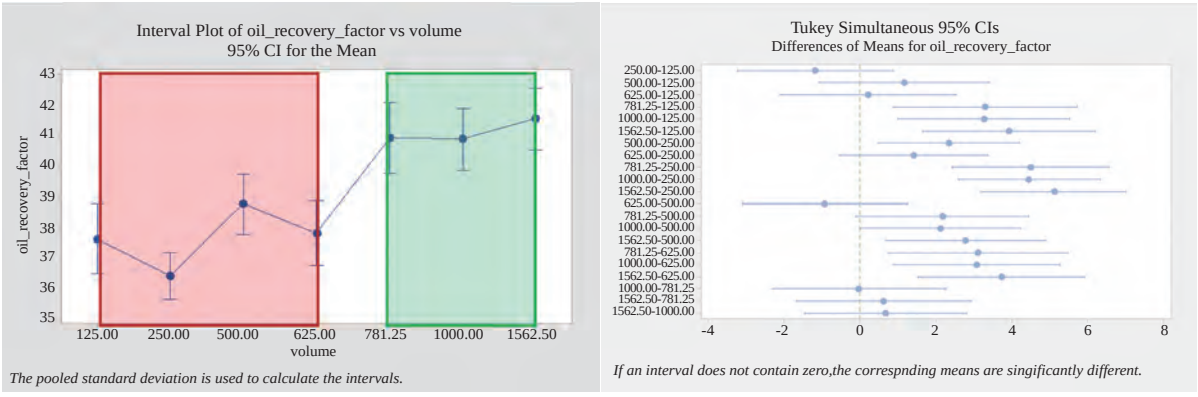

Figure 10
Interval Plot (Left) and Tukey Comparison (Right) - Oil Recovery and Grid Volume

The result of one-way ANOVA analysis between simulation material balance error and grid size is shown in Table 9. With a significant level of 0.05, the null hypothesis was also rejected because of the same reason as given above. Tukey comparison also showed two distinct groups: (i) red shade, from 125 to 781.25 m^3, and (ii) green shade, from 781.25 to 1,562.50 m^3. Moreover, when grid volume is increased, material balance error increased, which can lead to unreasonable simulation results and misinterpretation of smart waterflooding behaviour. The smaller grid volume requires more computational time. The biggest grid size with the same material balance error as the smallest one (red shade) was also selected. After integrating results from material balance error and oil recovery, we observed that the optimum grid size is 625 m^3.

Table 9
Grid Size Influence: Simulation Material Balance Error – ANOVA Result

Source	Degree of freedom	Sum of squares	Means squares	*F* value	*P* value
Volume	6	1,628	271.31	5.80	<<0.001
Error	662	31,003	46.76		
Total	668	32,631			

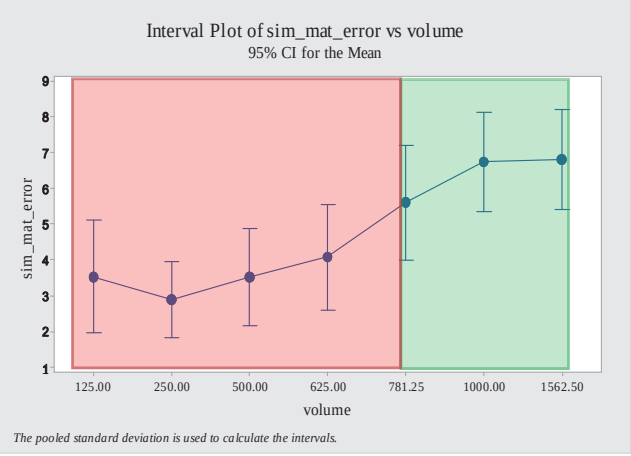

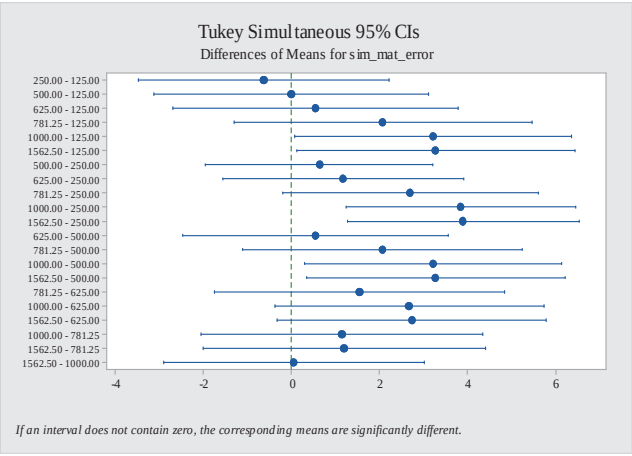

Figure 11
Interval Plot (Left) and Tukey Comparison (Right) - Simulation Material Balance Error and Grid Volume

The result of one-way ANOVA analysis between simulation time and grid size is shown in Table 10. The null hypothesis was also rejected, and further analysis by Tukey comparison (shown in Figure 12), showed that there is no significant difference in simulation time between 500 and 625 m^3 and from 781.25 to 1,000 m^3 grid volume. Thus, integrating all the results from these three analysis (i) grid size influence: oil recovery, (ii) grid size influence: simulation material balance error, and (iii) grid size influence: simulation time; we observed that there is no significant difference in oil recovery, simulation material balance error, or simulation time between grid volume 500 and 625 m^3. Hence, this grid volume range was selected as the optimized grid size.

Table 10
Grid Size Influence: Simulation Time – ANOVA Result

Source	Degree of freedom	Sum of squares	Means squares	*F* value	*P* value
Volume	6	1,038,9355,661	1,731,559,277	1,642.59	<<0.001
Error	662	698,909,178	1,054,162		
Total	668	11,088,264,839			

2.2.2 Heterogeneity Effect on Smart Waterflooding

This sensitivity analysis used one factor, porosity variance, with four levels: 0.0001, 0.001, 0.01, and 0.1. A repetitive observation was generated by multiple realizations as previously mentioned. The analysis is conducted in two sections: (i) heterogeneity effects on oil recovery, and (ii) heterogeneity effects on water cut (after 20 years of simulation).

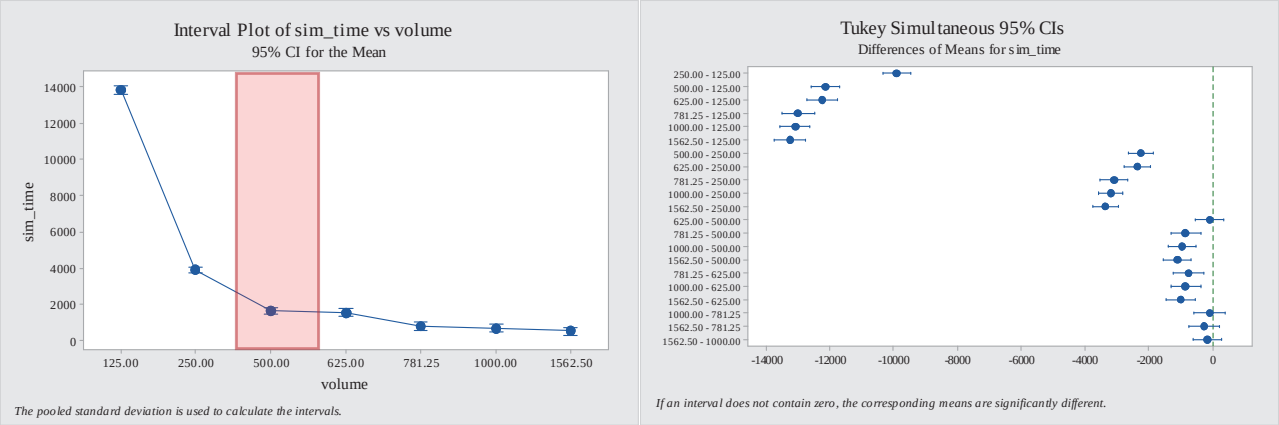

Figure 12
Interval Plot (Left) and Tukey Comparison (Right) - Simulation Time and Grid Volume

The result of one-way ANOVA analysis between oil recovery and porosity variance is shown in Table 11. The null hypothesis was rejected because the critical F-values is 2.641, which is comparably lower than the calculated F-values in Table 11. Sequentially, we performed a Tukey comparison, from Figure 13, it could be deduced that there was no statistical difference between porosity variance from 0.0001 to 0.001 and from 0.01 to 0.1. The range that exhibited a significant difference is 0.001 to 0.01, as shown in red (Figure 13).

Table 11
Heterogeneity Influence: Oil Recovery – ANOVA Result

Source	Degree of freedom	Sum of squares	Means squares	*F* value	*P* value
Variance	3	32,858,198	10,952,733	155.92	<<0.001
Error	370	25,990,272	70,244		
Total	373	58,848,470			

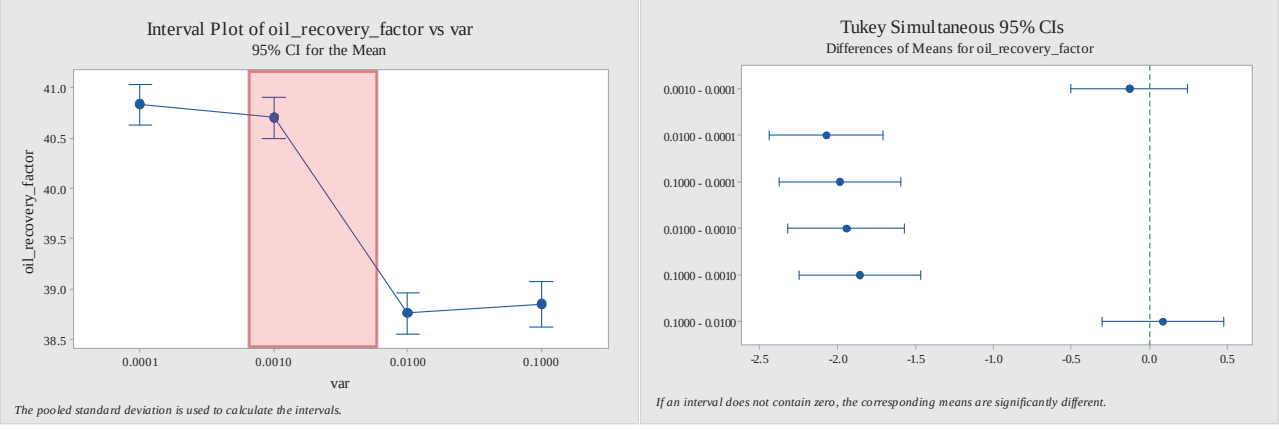

Figure 13
Interval Plot (Left) and Tukey Comparison (Right) – Oil Recovery and Porosity Variance

The result of one-way ANOVA analysis between water cut (WCUT) and porosity variance is shown in Table 12. The null hypothesis was also rejected and Tukey comparison in Figure 14 showed a significant difference in porosity variance ranging from 0.001 to 0.01, as shown in red (Figure 14).

Table 12
Heterogeneity Influence: WCUT – ANOVA Result

Source	Degree of freedom	Sum of squares	Means squares	*F* value	*P* value
Variance	3	32,858,198	10,952,733	155.92	<<0.001
Error	370	25,990,272	70,244		
Total	373	58,848,470			

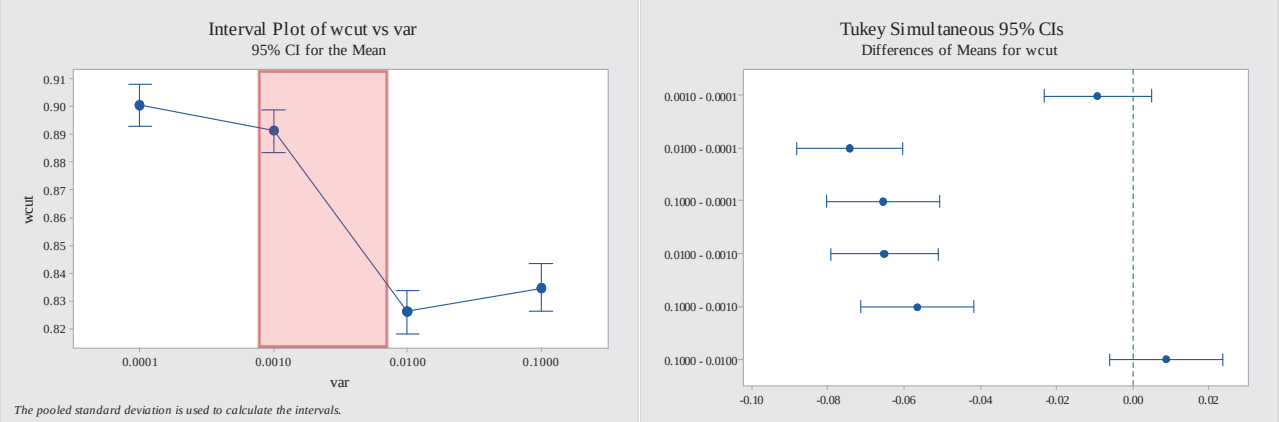

Figure 14
Interval Plot (Left) and Tukey Comparison (Right) – WCUT and Porosity Variance

In summary, the porosity variance range (0.001-0.01) seems to affect smart waterflooding oil recovery and WCUT performance. It appears that the model is fully heterogeneous at porosity variance of 0.01 and a porosity variance value greater than 0.01 could not further alter smart waterflooding behaviour. On the other hand, when porosity variance was 0.001, the model was nearly homogeneous. Thus, a system with a porosity variance less than 0.001 is estimated as a homogenized system. This result shows that heterogeneity statistically affects smart waterflooding within a certain range. Kadeethum et al.[30] explain that heterogeneity has a direct influence on CEC, and consequently affects the interpolant value. Meanwhile, the interpolant was used to represent the wettability changes in the smart waterflooding system. This means that the interdependency of the wettability changes in CEC and heterogeneity can alter the overall system performance.

CONCLUSION

A validation of coreflooding results has been conducted to investigate uncertainties of smart waterflooding in a core-scale. Subsequently, the validated model was extended to 3-D model to evaluate smart waterflooding in the field-scale. Also, the uncertainties of smart waterflooding from core- to field-scale have been assessed. Taking into consideration the limitations and assumptions made in this study, the following conclusions are drawn:

- There are many realizations that can mimic the smart waterflooding experiment. For the range of uncertainties, only one validated model may not be sufficient because each validated model can lead to different results in the 3-D model.
- Three types of geochemical reactions: (i) intra-aqueous, (ii) mineral dissolution/precipitation, and (iii) ion-exchange reactions were required to describe smart waterflooding behaviour.
- Grid size affects smart waterflooding performance. Grid volume of 500 to 625 m^3 is identified as an optimum grid size that can accommodate reasonable material balance error and simulation time.
- Heterogeneity directly influences CEC, which affects the interpolanted value and subsequently affects smart waterflooding performance.
- Porosity variance range of 0.001 to 0.01 influences smart waterflooding. Porosity variance outside this range cannot further alter smart waterflooding performance.

RECOMMENDATIONS

Several pertinent issues were not included in this study and should be considered in future studies. Examples of such matters include the following:

- Effect of grid size is accounted as the grid volume. However, each dimension (i.e. d*x*, d*y*, and d*z*) effect should be analysed separately.
- Incorporation of capillary pressure in the simulation model.

REFERENCES

[1] Martin J. (1959). *The effects of clay on the displacement of heavy oil by water*. Retrieved from http://dx.doi.org/10.2118/1411-G

[2] Bernard, G. G. (1967). *Effect of floodwater salinity on recovery of oil from cores containing clays.* SPE 1725. Retrieved from http://dx.doi.org/10.2118/1725-MS

[3] Tang, G., & Morrow, N. (1997). Salinity, temperature, oil composition and oil recovery by waterflooding. *SPE Reservoir Engineering, 12*(4), 269-276.

[4] Morrow, N., Tang, G., Valat, M., & Xie, X. (1998). Prospects of improved oil recovery related to wettability and brine composition. *Journal of Petroleum and Engineering, 20*(3-4), 267-276.

[5] Zhang, Y., & Morrow, N. (2006). *Comparison of secondary and tertiary recovery with change in injection brine composition for crude oil/ sandstone combinations.* Presented at the SPE/DOE Symposium on Improved Oil Recovery. Tulsa, USA: Society of Petroleum Engineers.

[6] Zhang, Y., Xie, X., & Morrow, N. (2007). *Waterflood performance by injection of brine with different salinity for reservoir cores.* Presented at the SPE Annual Technical Conference and Exhibition, 11-14 November. Anaheim, CA, USA: Society of Petroleum Engineers.

[7] Lager, A., Webb, K., Black, C., Singleton, M., & Sorbie, K. (2008a). Low-salinity oil recovery—An experimental investigation. *Petrophysics, 49*(1), 28-35.

[8] Rivet, S., Lake, L., & Pope, G. (2010). *A coreflood investigation of low salinity enhanced oil recovery.* Presented at SPE Annual Technical Conference and Exhibition, 19-22 September. Florence, Italy: Society of Petroleum Engineers.

[9] Winoto, W., Loahardjo, N., Xie, S. X., Yin, P., & Morrow, N. R. (2012). *Secondary and tertiary recovery of crude oil from outcrop and reservoir rocks by low salinity waterflooding.* Presented at SPE Improved Oil Recovery Symposium, 14-18 April. Tulsa, Oklahoma, USA: Society of Petroleum Engineers.

[10] Kozaki, C. (2012). *Efficiency of low salinity polymer flooding in sandstone cores* (M.Sc. thesis). University of Texas at Austin.

[11] Awolayo, A. N., Sarma, H. K., & Al-Sumaiti, A. M. (2014a). *An experimental study of smart waterflooding on fractured carbonate reservoirs.* Proceedings from ASME 2014 33rd International Conference on Ocean, Offshore and Arctic Engineering, San Francisco, USA: American Society of Mechanical Engineers.

[12] Awolayo, A. N., Sarma, H. K., & Al-Sumaiti, A. M. (2014b). *A laboratory study of ionic effect of smart water for enhancing oil recovery in carbonate reservoirs.* Proceedings from SPE EOR Conference at Oil and Gas West Asia, Muscat, Oman, Vol. SPE 169662: Society of Petroleum Engineers.

[13] Xie, Q., Ma, D., Wu, J., Liu, Q., Jia, N., & Luo, M. (2015). *Low salinity waterflooding in low permeability sandstone: Coreflood experiments and interpretation by thermodynamics and simulation.* Presented at SPE Asia Pacific Enhanced Oil Recovery Conference, 11-13 August. Kuala Lumpur, Malaysia: Society of Petroleum Engineers.

[14] Dang, C. (2015). *Mechanistic modeling, design, and optimization of low salinity waterflooding.* Calgary, Alberta, Canada (Ph.D. thesis). University of Calgary.

[15] Hamon, G. (2016). Low-salinity waterflooding: Facts, inconsistencies and the way forward. *Society of Petrophysicists and Well-Log Analysts, 57*(1).

[16] Webb, K. J., Black, C. J. J., & Al-Ajeel, H. (2004). *Low salinity oil recovery-log-inject-log.* Proc., SPE/DOE Symposium on Improved Oil Recovery, Tulsa, Oklahoma, USA, 17-21 April. SPE-89379-MS

[17] Lager, A., Webb, K. J., Collins, I. R., & Richmond, D. M. (2008b). *LoSal enhanced oil recovery: Evidence of enhanced oil recovery at the reservoir scale.* Paper SPE 113976 Presented at the SPE/DOE Improved Oil Recovery Symposium, Tulsa, Oklahoma, USA, 19-23 April.

[18] Mahani, H., Sorop, T. G., Ligthelm, D., Brooks, D., Vledder, P., Mozahem, F., & Ali, Y. (2011). *Analysis of field responses to low-salinity waterflooding in secondary and tertiary mode in Syria.* Paper SPE 142960 Presented at the SPE EUROPEC/EAGE Annual Conference and Exhibition, 23-26 May, Vienna, Austria.

[19] Willhite, G. (1986). *Waterflooding spe textbook series vol. 3.* Kuala Lumpur, Malaysia: Society of Petroleum Engineering.

[20] Moreno, J. E., & Flew, S. (2011). *EOR: Challenges of translating fine scale displacement into full field Models.* Presented at SPE Enhanced Oil Recovery Conference, 19-21 July. Kuala Lumpur, Malaysia: Society of Petroleum Engineers.

[21] Moreno, J. E., Flew, S., & Gurpinar, O. (2013). *EOR: Challenges of translating fine scale displacement into full field models -Part 2.* Presented at SPE Enhanced Oil Recovery Conference, 2-4 July. Kuala Lumpur, Malaysia: Society of Petroleum Engineers.

[22] Moreno, J. E., Flew, S., & Gurpinar, O. (2015). *EOR: Challenges of translating fine scale displacement into full field models part 3*. Presented at SPE Asia Pacific Enhanced Oil Recovery Conference, 11-13 *August.* Kuala Lumpur, Malaysia: Society of Petroleum Engineers.

[23] Kadeethum, T. (2016). *Understanding uncertainties using performance predictive models for smart waterflooding* (M.Sc. thesis). Calgary, Alberta, Canada: University of Calgary.

[24] Al-Shalabi, E. W. (2014). *Modeling the Effect of Injecting Low Salinity Water on Oil Recovery* (Ph.D. thesis). Austin, Texas, USA: The University of Texas at Austin.

[25] Korrani, A. K. (2014). *Mechanistic modeling of low salinity water injection* (Ph.D. thesis). Austin, Texas, USA: The University of Texas at Austin.

[26] Awolayo, A., Sarma, H., & Nghiem, L. (2017). *A comprehensive geochemical-based approach at modeling and interpreting brine dilution in carbonate reservoirs.* Presented at SPE Reservoir Simulation Conference, 20-22 February 2017. Montgomery, TX, USA: Society of Petroleum Engineers.

[27] Bethke, C. (2006). *GWB essentials guide.* Illinois, USA: University of Illinois.

[28] Nghiem, L., Sammon, P., Grabenstetter, J., & Ohkuma, H. (2004). *Modeling CO_2 storage in aquifers with a fully-coupled geochemical EOS compositional simulator.* Proceedings from SPE/DOE symposium on improved oil recovery, *Tulsa, Oklahoma*. SPE-89474-MS: Society of Petroleum Engineers.

[29] Jerauld, G., Lin, C., Webb, K., & Seccombe, J. (2008). Modeling low salinity waterflooding. *SPE Reservoir Engineering, 11*(6), 1000-1012.

[30] Kadeethum, T., Sarma, H., & Maini, B. (2017). *Enhance microscopic sweep efficiency by smart water in tight and very tight oil reservoirs.* Presented at SPE Canada Unconventional Resources Conference, 15-16 February Calgary, Canada: Society of Petroleum Engineers.

[31] Breeuwsma A., Wosten J. H. M., Vleeshouwer, J. J., Slobbe V., & Bouma, J. (1986). Derivation of land qualities to assess environmental problem from the soil survey. *Soil Science Society of America Journal, 50,* 186-190.

[32] GEM. (2015). GEM user guide - version 2015. *Computer Modelling Group (CMG)*, 691.

[33] Timur, A. (1968). An investigation of permeability, porosity, & residual water saturation relationships for sandstone reservoirs. *The Log Analyst, 9*(4).

[34] Brooks, R., & Corey, A. (1964). *Hydraulic properties of porous media* (p.24). Hydrology Papers. Hydrology Papers, Colorado State University.

[35] Levine, D., Ramsey, P., & Smidt, R. (2001). *Applied statistics for engineering and scientists.* Pearson Education.

[36] Liu, Y., & Yang, Y. (2015). Evolution of the surface area of limestone during calcination and sintering. *Journal of Power and Energy Engineering*, 56-62.

[37] Loahardjo, N., Xie, X., & Morrow, N. (2010). Oil recovery by sequential waterflooding of mixed-wet sandstone and limestone. *Energy & Fuels, 24*(9), 5073-5080.

[38] Morrow, N., Valat, M., & Yidliz, H. (1996). *Effect of brine composition on recovery of an Alaskan crude oil by waterflooding.* Presented at Annual Technical Meeting, June 10-12. Calgary, Alterta: Petroleum Society of Canada.

[39] Schott, J., Brantley, S., Crerar, D., Guy, C., Maria, B., & Willaime, C. (1989). Dissolution kinetics of strained calcite. *Geochimica et Cosmochimica Acta*, 373-382.

